

Cloud Color and Ocean Radiant Heating

DAVID A. SIEGEL,* TOBY K. WESTBERRY, AND J. CARTER OHLMANN

*Institute for Computational Earth System Science, University of California, Santa Barbara,
Santa Barbara, California*

(Manuscript received 11 October 1996, in final form 26 May 1998)

ABSTRACT

It is well recognized that clouds regulate the flux of solar radiation reaching the sea surface. Clouds also affect the spectral distribution of incident irradiance. Observations of spectral and total incident solar irradiance made from the western equatorial Pacific Ocean are used to investigate the "color" of clouds and to evaluate its role in upper-ocean radiant heating. Under a cloudy sky, values of the near-ultraviolet to green spectral irradiance are a significantly larger fraction of their clear-sky flux than are corresponding clear-sky fractions calculated for the total solar flux. For example, when the total solar flux is reduced by clouds to one-half of that for a clear sky, the near-ultraviolet spectral flux is only reduced ~35% from its clear-sky value. An empirical parameterization of the spectral cloud index is developed from field observations and is verified using a plane-parallel, cloudy-sky radiative transfer model. The implications of cloud color on the determination of ocean radiant heating rates and solar radiation transmission are assessed using both model results and field determinations. The radiant heating rate of the upper 10 cm of the ocean (normalized to the climatological incident solar flux) may be reduced by a factor of 2 in the presence of clouds. This occurs because the near-infrared wavelengths of solar radiation, which are preferentially attenuated by clouds, are absorbed within the upper 10 cm or so of the ocean while the near-ultraviolet and blue spectral bands propagate farther within the water column. The transmission of the solar radiative flux to depth is found to increase under a cloudy sky. The results of this study strongly indicate that clouds must be included in the specification of ocean radiant heating rates for air-sea interaction studies.

1. Introduction

It is obvious that clouds regulate the total flux of solar radiation incident on the sea surface. Clouds also have a significant impact upon the spectral distribution of the incident irradiance (e.g., Middleton 1954; Siegel and Dickey 1987; Nann and Riordan 1991; Ohlmann et al. 1996; Ohlmann et al. 1998). Clouds reduce the quantity of solar radiation reaching the earth's surface by reflecting incident energy back to space and by increasing the probability that a photon is attenuated before reaching the earth's surface. Clouds impart a spectral signature different from the clear-sky case as photon interactions with cloud droplets are introduced. Under maritime clear-sky conditions, the spectral signature of the incident irradiance is determined primarily by Ray-

leigh scattering and molecular absorption. As a cloud's optical thickness increases, so does the probability of absorption and scattering by cloud water droplets and the clear-sky atmosphere. Absorption will be particularly significant for the near-infrared spectral region while Rayleigh scattering will be the dominant process in the blue (e.g., Liou 1980; Nann and Riordan 1991; O'Hirok and Gautier 1998a,b). Hence, one should expect increased attenuation by clouds of the longer wavelengths of solar radiation. Last, cloud layers can reflect back to the sea surface photons that have been already reflected by the air-sea interface or backscattered from within the ocean (Middleton 1954). As the sea surface albedo is greatest in the blue-green spectral region (e.g., Katsaros et al. 1985; Ohlmann 1997), this represents an additional enhancement of short wavelength visible energy. The combination of these processes indicate that the incident irradiance spectrum under a cloudy sky will be bluer than for a clear-sky spectrum.

The relative blueing of the solar radiation spectrum for a cloudy sky may have an important role in the radiant heating of the upper layers of the ocean. Vertical decay rates for in-water solar radiation attenuation are much greater for the near-infrared wavelengths than for the near-ultraviolet and short-wavelength visible spectral regions (e.g., Jerlov 1976; Woods et al. 1984).

* Additional affiliation: Department of Geography, and Bren School of Environmental Science and Management, University of California, Santa Barbara, Santa Barbara, California.

Corresponding author address: Dr. David A. Siegel, Institute for Computational Earth System Science, University of California, Santa Barbara, Santa Barbara, CA 93106-3060.
E-mail: davey@icess.ucsb.edu

Hence, changes in the spectral composition of the in situ irradiance distribution may have a role in determining radiant heating rates for the upper ocean. In broad terms, the redder the incident solar spectrum, the more radiation will be absorbed in the upper few meters of the sea; whereas the bluer the incident spectrum, the greater the flux that can penetrate within the water column. By altering the spectral composition of the incident irradiance spectrum, clouds potentially play an important role in regulating the vertical divergence of the in-water solar flux and, thereby, rates of ocean radiant heating.

In the following, we present measurements of total and spectral incident irradiance from the western equatorial Pacific Ocean to demonstrate the existence and significance of cloud color to ocean radiant heating. A simple parameterization for cloud color is developed and validated using a plane-parallel, cloudy-sky radiative transfer model. Finally, models of ocean radiation penetration, as well as in situ spectroradiometric observations, are used to quantify the role of cloud color on solar radiation penetration fluxes and ocean radiant heating rates.

2. Data and methods

The Tropical Ocean Global Atmosphere (TOGA) Coupled Ocean–Atmosphere Response Experiment (COARE) was conducted in the western equatorial Pacific Ocean to address air–sea coupling processes within the warm pool (cf. Webster and Lukas 1992). The intensive observation period of TOGA COARE was performed from 1 October 1992 to 28 February 1993 within a domain centered approximately at 2°S, 156°E. Of present interest are shipboard observations of incident solar flux and upper-ocean optical, physical, and biological parameters made from the R/V *John Vickers* between 21 December 1992 and 19 January 1993, taken within 5 km of 2.08°S, 156.25°E (Siegel et al. 1995a; Ohlmann et al. 1998).

A spectroradiometer system, based upon a Biospherical Instruments MER-2040 (San Diego, California), was developed and deployed for this experiment (Siegel et al. 1995a). Irradiance spectra were sampled simultaneously from a spectroradiometer mounted on the ship's mast and underwater using an identical system that profiles from the sea surface to 200-m depth. The spectroradiometer measures downwelling, $E_d(z, \lambda)$, and upwelling, $E_u(z, \lambda)$, irradiance spectra in 13 discrete wavebands (with center wavelengths of 340, 380, 412, 441, 465, 490, 520, 540, 560, 589, 625, 665, and 683 nm). The mast-mounted spectroradiometer measured only $E_d(0^+, \lambda)$. The nominal half-power bandwidth is 10 nm for each channel and out-of-band rejection rates are typically greater than 1 000 000:1. Extensive efforts were expended on the optical characterization of the ultraviolet-transmitting diffuser, including determinations of in-air and in-water cosine response, spectral

response of each channel, immersion coefficient, dark current variation with temperature, and diffuser pressure effects (Siegel et al. 1995a). The spectroradiometer was calibrated at the University of California, Santa Barbara using a standard lamp directly traceable to the National Institute of Standards and Technology. An Eppley Laboratories (Newport, Rhode Island) PSP pyranometer was deployed next to the surface spectroradiometer to determine the total incident solar flux (250–2500 nm). This instrument was calibrated before and after our TOGA COARE observations at Eppley Laboratories. Data from the underwater spectroradiometer system were recorded at a rate of 4 Hz while profiling at speeds of 0.5–0.7 m s⁻¹, resulting in a vertical sampling of 5–8 samples per meter. Data were subsequently binned into 1-m vertical bins following procedures and software presented by Siegel et al. (1995b).

The profiling spectroradiometer system was interfaced with several other instruments: a chlorophyll fluorometer (SeaTech, Corvallis, Oregon), a beam transmissometer (660 nm, 25-cm path length; SeaTech, Corvallis, Oregon), and conductivity and temperature probes (SeaBird, Bellevue, Washington). Both the profiling and mast-mounted systems were equipped with sensors for the measurement of package tilt and roll (rms precision of $\pm 2^\circ$ for frequencies less than 0.2 Hz). More than 1500 casts were made with a temporal sampling interval between casts of ~ 20 min. Visual cloud observations were made with each spectroradiometer cast, corresponding to roughly 30 each day, and a fish-eye lens video camera was mounted on the mast, enabling continuous records of cloud cover to be obtained. The all-sky video data were used to validate the visual cloud observations as well as to verify clear-sky conditions for assessing the clear-sky irradiance model. Finally, seawater samples were collected twice per day for analysis of chlorophyll *a* and pheopigment concentrations using standard fluorometric techniques.

The spectral and total incident irradiance spectra collected during TOGA COARE were modeled using a recent implementation of the discrete ordinate radiative transfer model for clear and cloudy skies (SBDART; Ricchiuzzi et al. 1998). This implementation includes the effects of aerosol scattering, cloud droplet absorption and scattering, and molecular absorption. The SBDART model calculates bidirectional reflectance for a vertically inhomogeneous plane-parallel medium, enabling the determination of incident solar spectra for both cloudy and clear skies (Ricchiuzzi et al. 1998). Twice daily vertical profiles of atmospheric water vapor from the R/V *Moana Wave* (located ~ 50 km northeast of the R/V *John Vickers*) were used in specifying clear-sky irradiance spectra. The mean total water vapor content for the period of our observations (21 December 1992–11 January 1993) was equal to 5.39 (± 0.68 std dev) g cm⁻² compared with a standard tropical atmosphere of 4.12 g cm⁻² (McClatchey et al. 1972). Columnar ozone concentrations were taken from Total

TABLE 1. Comparison of modeled and observed clear-sky spectra. Units are $\mu\text{W cm}^2 \text{ nm}^{-1}$ for each of the individual spectral wavebands and W m^{-2} for the total solar flux ($1 \text{ W m}^2 \text{ nm}^{-1} = 100 \mu\text{W cm}^2 \text{ nm}^{-1}$). Bias is defined as observed flux minus the modeled flux and the root-mean-square deviation is denoted as rms. Normalization is done using the observed mean flux. A total of 6580 5-s mean observations compose the clear-sky dataset.

Waveband (nm)	Observed mean	Mean bias	Normalized bias (%)	Rms deviation	Normalized rms (%)
340	36.27	-1.41	-3.89	2.10	5.78
380	48.70	3.04	6.24	3.47	7.12
410	82.84	2.53	3.05	5.92	7.14
440	93.81	2.76	2.94	7.17	7.64
465	104.64	2.68	2.56	8.29	7.92
490	103.57	5.17	4.99	8.83	8.52
520	96.91	2.61	2.69	8.31	8.57
540	99.23	2.75	2.77	8.67	8.73
565	97.40	4.06	4.16	8.73	8.96
590	92.30	4.08	4.42	8.39	9.09
625	88.61	0.35	0.39	8.15	9.20
665	85.69	1.06	1.23	8.06	9.40
683	77.42	-3.77	-4.88	7.59	9.81
total	562.09	-10.34	-1.84	45.83	8.15

Ozone Mapping Scanner observations for the 1° square containing the R/V *John Vickers*. The mean columnar ozone was equal to $0.244 (\pm 0.066 \text{ std dev})$ atmospheric centimeter (atm cm), which is nearly the same as the standard tropical atmosphere (0.247 atm cm). Aerosols were assumed to be an oceanic type and the visibility was taken to be 23 km. Modeled clear-sky fluxes did not change significantly with considerable differences in visibility. Cloudy-sky spectra were calculated for a variety of cloud optical thicknesses using a single 2-km-thick cloud layer with a base height of 1 km and an effective cloud droplet radius of $25 \mu\text{m}$. Reasonable variations in the cloud-base height, layer thickness, and effective cloud droplet radius had minimal effects on the resulting incident spectral fluxes (typically less than 1%; data not shown).

In order to validate the modeling of clear-sky irradiance spectra, the model results were compared with "clear-sky" data culled from the present observations. The clear-sky dataset was selected based upon at-sea visual cloud observations and a subjective analysis of the fish-eye cloud video record. A total of 6580 individual 5-s mean observations make up the clear-sky dataset. The comparison statistics between the modeled and observed clear-sky spectral irradiance and clear-sky total solar flux determinations are presented in Table 1. Generally, the comparison between the modeled and observed clear-sky spectra is very good with normalized mean biases (observation minus model normalized with the observed value) within 5% of the observed value and normalized rms errors within 10%. For the total flux, the clear-sky modeled fluxes are slightly higher than observed (Table 1). The comparison is slightly better if only observations with solar zenith angles less than 45° are used (normalized rms deviations range from 3.7% to 5.4% and normalized biases are slightly smaller compared with the total clear-sky dataset; results not shown). For the high solar zenith angle observations

($>45^\circ$), the normalized biases are similar to the total dataset results, but the rms deviations are larger (10%–20%). Although the rms deviations for low solar elevations are larger than the total clear-sky dataset results (which may be due to ship roll, time mismatches, etc.), the consistency in the normalized mean biases suggest that the clear-sky model is excellent for our purposes. These error bounds are also excellent considering that no temporal averaging is performed to remove ship roll effects beyond the 5-s averaging. Direct examination shows ship roll-induced variability to be less than 5% of the observed value (not shown). In summary, the modeled clear-sky fluxes compare well with clear-sky observations of spectral and total solar irradiance, validating its use in the present study.

3. Temporal variability of cloud indices during TOGA COARE

Time series of total solar irradiance $\overline{E}_d(0^+)$ and the modeled clear-sky flux $\overline{E}_{CS}(0^+)$ show the expected range of daily variations (Fig. 1a). For the most part, values of the measured flux $\overline{E}_d(0^+)$ are smaller than the modeled clear-sky flux $\overline{E}_{CS}(0^+)$. However, the measured flux is often greater than $\overline{E}_{CS}(0^+)$. This suggests a local intensification in the solar flux due to 3D cloud effects (e.g., Byrne et al. 1996; O'Hirok and Gautier 1998a). This interpretation is also supported by the probability distributions that show maximum values of $\overline{E}_{CS}(0^+)$ slightly less than 1000 W m^{-2} , whereas values of $\overline{E}_d(0^+)$ are often observed greater than this maximum clear-sky value (Fig. 2).

The comparison between $\overline{E}_d(0^+)$ and $\overline{E}_{CS}(0^+)$ can be conveniently cast as a single parameter, the cloud index $\overline{\text{CL}}$, or

$$\overline{\text{CL}} = [\overline{E}_{CS}(0^+) - \overline{E}_d(0^+)]/\overline{E}_{CS}(0^+), \quad (1)$$

where the value of $\overline{\text{CL}}$ is equal to 0 for a clear-sky and

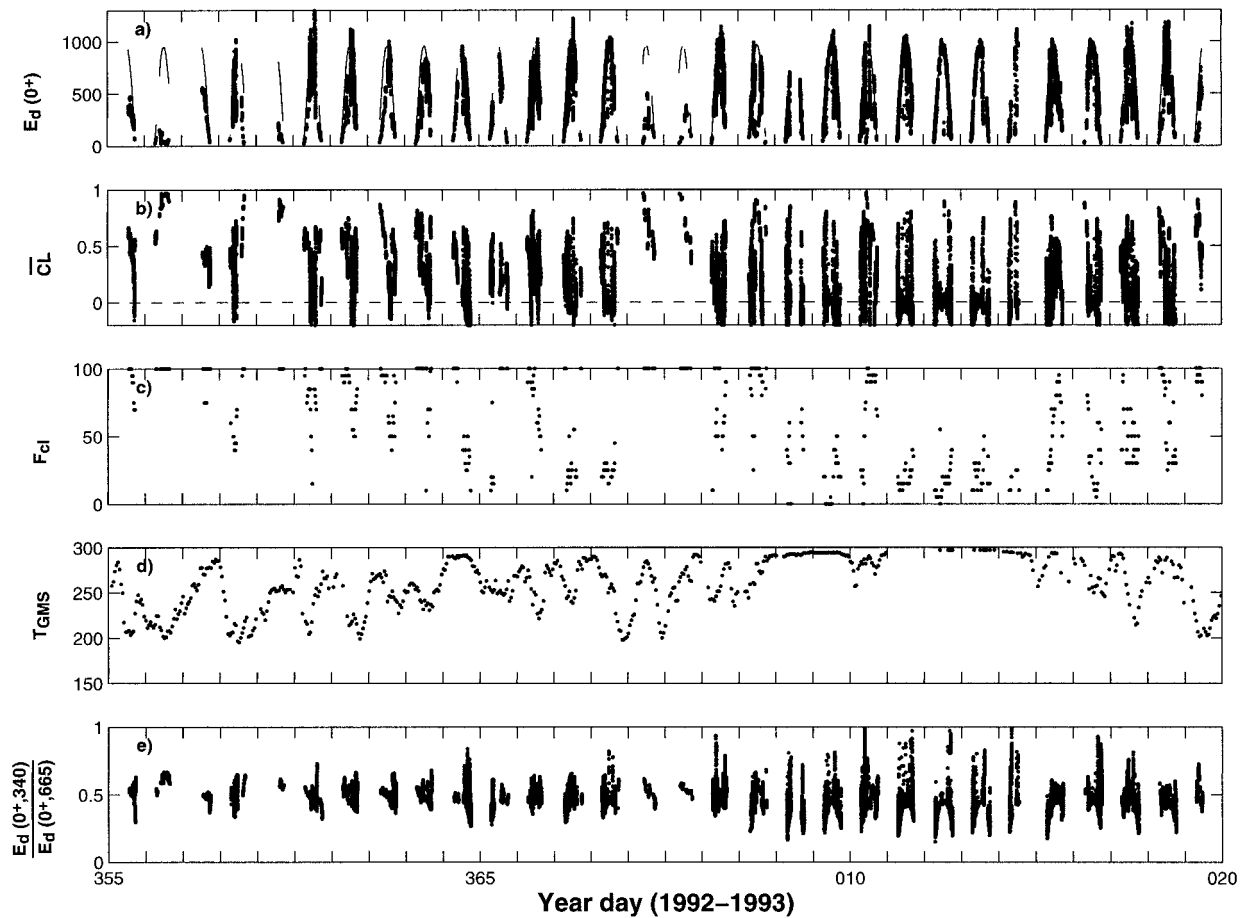


FIG. 1. Time series of (a) $\overline{E}_d(0^+)$ (individual dots; W m^{-2}) and $\overline{E}_{cs}(0^+)$ (thin solid line; W m^{-2}), (b) \overline{CL} [$= 1 - \overline{E}_d(0^+)/\overline{E}_{cs}(0^+)$] and (c) fractional cloud coverage visual observations, F_{cl} , from the R/V *John Vickers* during TOGA COARE, (d) cloud-top temperatures from the GMS (Japan) satellite, T_{GMS} (K), and (e) the spectral ratio of $E_d(0^+, 340)$ to $E_d(0^+, 665)$. Time is in local days. Time gaps are due to the fact that incident spectral irradiance measurements were not made when the underwater spectroradiometer system was not operating (see Siegel et al. 1995a for more details). The GMS cloud-top temperature estimates are centered at the location of the R/V *John Vickers* and are averaged over a pixel extent of 50 km. Values of \overline{CL} are calculated only if $\overline{E}_d(0^+) \geq 25 \text{ W m}^{-2}$. The minimum solar zenith angle during these observations is 19° .

is equal to 1 for a totally opaque sky (e.g., Gautier and Frouin 1992). Values of \overline{CL} are calculated only if the total solar flux $\overline{E}_d(0^+)$ is greater than 25 W m^{-2} . The cloud index time series shows a large degree of variability with many periods of high and low \overline{CL} values (Fig. 1b). No statistically significant diurnal variations in \overline{CL} were found, implying that changes in solar zenith angle are not an obvious component of \overline{CL} variability. Negative values of \overline{CL} make up 26% of the observations (10% of the observations have \overline{CL} less than -0.1) and are likely due to the cloud-edge reflections. The mode of the \overline{CL} distribution occurs for a \overline{CL} value of 0 while the distribution of \overline{CL} values between 0.1 and 1.0 is almost uniform (Fig. 2).

Visual cloud observations provide a measure of fractional cloud coverage, F_{cl} , to compare with our nearly instantaneous, point estimate of cloud radiometric effects, \overline{CL} . Temporal variations in F_{cl} are roughly similar to those observed for \overline{CL} as days with high \overline{CL} values

have high fractional cloud coverage and vice versa (Fig. 1). Regression analysis among cloud indices (Table 2) shows substantial correspondence between instantaneous F_{cl} and \overline{CL} values ($r^2 = 0.40$) and between daily mean estimates ($r^2 = 0.67$). However, many obvious differences exist. First, temporal changes in F_{cl} are much smoother and more regular than those for \overline{CL} (Fig. 1). This can be observed in the lower regression coefficient values found for the instantaneous determinations compared with the daily mean regression coefficients (Table 2). Second, the distribution of F_{cl} occurrences shows that rarely are perfectly clear skies observed even though the mode of the \overline{CL} distribution is found for a value of 0 (Fig. 2).

Remotely sensed cloud-top temperatures from the Japanese Geosynchronous Meteorological Satellite (GMS), T_{GMS} , provide a larger-scale perspective of the local cloud field (e.g., Chen et al. 1995). Presumably, the higher (and thicker) the aggregate cloud field, the

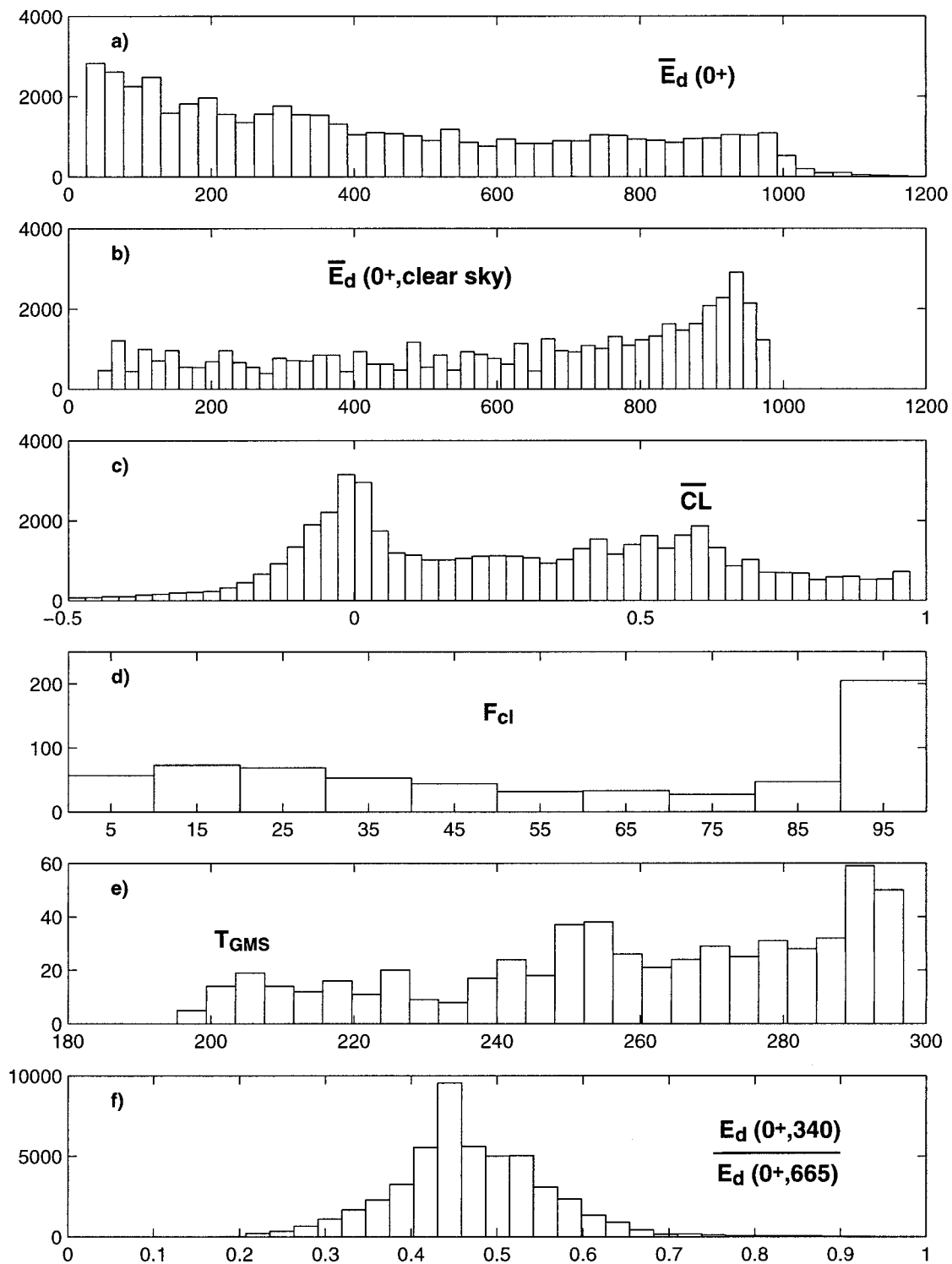


FIG. 2. Frequency of occurrences for (a) $\bar{E}_d(0^+)$, (b) $\bar{E}_{CS}(0^+)$, (c) \overline{CL} , (d) F_{cl} , (e) T_{GMS} , and (f) the spectral ratio of $E_d(0^+, 340)$ to $E_d(0^+, 665)$ evaluated over the entire dataset.

TABLE 2. Regression coefficients among various cloud indices. Regression coefficients (r) are calculated for the timescale at which the parameters are sampled and using daily mean parameter determinations (values shown in the parentheses). All regressions are significant at the 95% confidence interval [number of degrees of freedom are calculated following the procedure of Davis (1977)].

	\overline{CL}	F_{cl}	T_{GMS}
F_{cl}	0.632 (0.821)	—	—
T_{GMS}	-0.318 (-0.549)	-0.411 (-0.605)	—
$E_d(0^+, 340)/E_d(0^+, 665)$	0.742 (0.924)	0.424 (0.752)	-0.298 (-0.656)

lower the value of the cloud-top temperature; whereas when GMS temperatures approach 300 K, the sky should be cloud free. The GMS cloud-top temperature time series was created by sampling from a 50-km product centered on the location of the R/V *John Vickers*. Thus, these data should represent the cloud field on a larger scale than either the radiometric (\overline{CL}) or the visual (F_{cl}) cloud abundance estimates. The time series of GMS cloud-top temperature (Fig. 1d) show low-frequency variations that are roughly consistent with the \overline{CL} and F_{cl} observations (Figs. 1b and 1c) superimposed by hints of diurnal-scale changes presumably due to atmospheric convection. The time series of T_{GMS} is smoother than either \overline{CL} and F_{cl} as it represents the

cloud conditions averaged over a larger spatial region than either the radiometric or visual observations. The correlation coefficients (r) among are lower than those between \overline{CL} and F_{cl} (Table 2).

4. Spectral irradiance and clouds during TOGA COARE

Differences in the visible portion of the incident irradiance spectrum become apparent after they have been sorted by the value of the cloud index (Fig. 3). The absolute magnitudes of the incident irradiance spectra decrease as the \overline{CL} value increases in line with the expected decrease in incident irradiance caused by clouds.

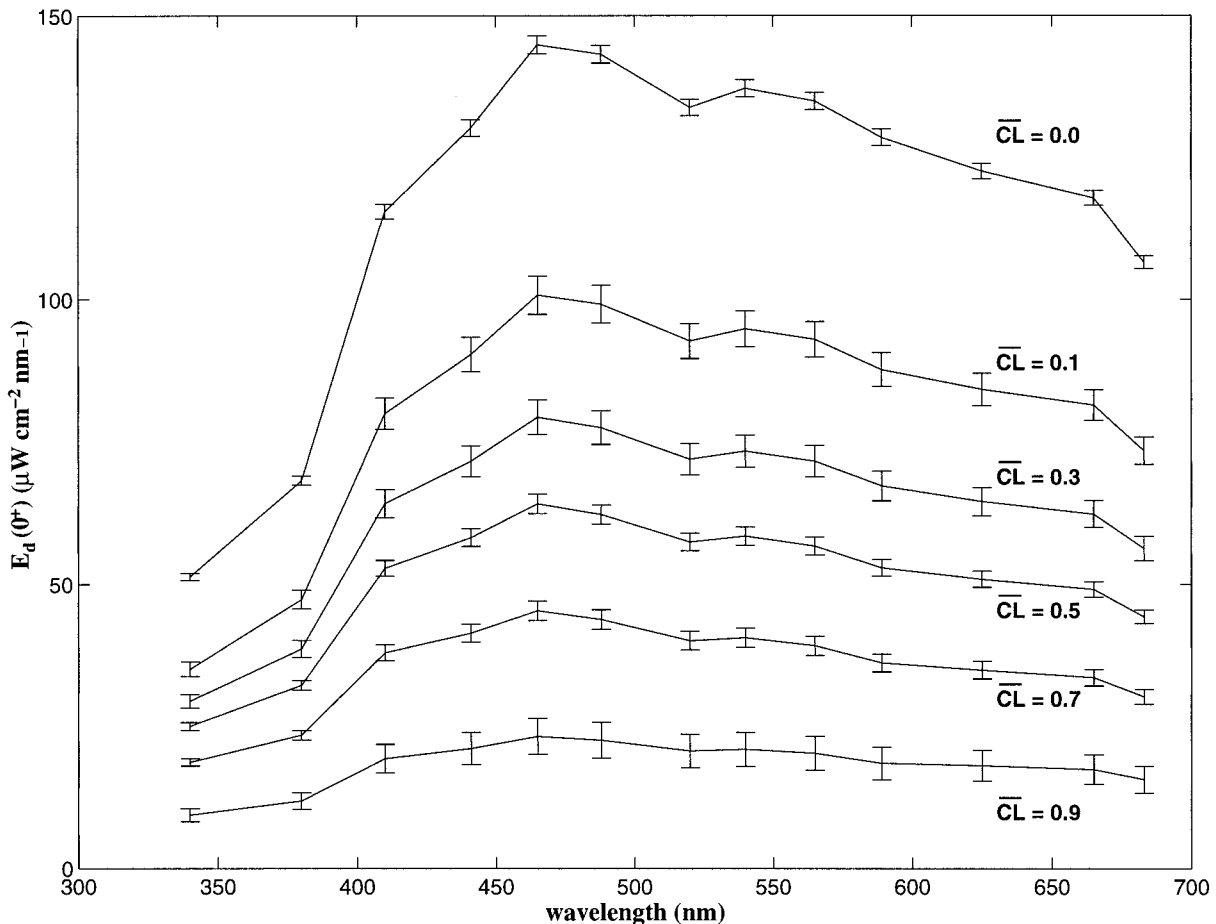


FIG. 3. Mean incident irradiance spectra $E_d(0^+, \lambda)$ for values of cloud index \overline{CL} ranging from 0–0.9. The vertical error bars represent 95% confidence intervals for the mean determinations. The \overline{CL} bin size $\Delta\overline{CL}$ is set to 0.02.

In addition, the shapes of the $E_d(0^+, \lambda)$ spectra become considerably flatter as the total cloud amount increases. This is the cloud-induced color signal that we are attempting to diagnose.

Changes in the shape of the incident irradiance spectrum can be assessed using the ratio of the near-ultraviolet, $E_d(0^+, 340 \text{ nm})$, and the red, $E_d(0^+, 665 \text{ nm})$, spectral irradiances (Fig. 1e). If the solar spectrum becomes bluer under cloudy conditions, the value of $E_d(0^+, 340)/E_d(0^+, 665)$ will increase as the cloud index increases. Under a clear sky ($-0.05 \leq \overline{\text{CL}} \leq 0.05$), the mean value of $E_d(0^+, 340)/E_d(0^+, 665)$ is equal to 0.42 (± 0.05 std dev, $N = 9007$), whereas under a cloudy sky ($0.85 \leq \overline{\text{CL}} \leq 0.95$) the mean value for this ratio is 0.59 (± 0.05 std dev, $N = 1824$). Hence, this ratio appears to be a good, simple discriminator of cloudy-sky conditions. For example, values of $E_d(0^+, 340)/E_d(0^+, 665)$ are significantly correlated [at 95% confidence interval (c.i.)] with determinations of $\overline{\text{CL}}$ on a per determination and a per day basis, explaining 55% and 85% of the variance, respectively (Table 2). However, the diurnal cycles in this ratio observed for clear-sky days confound this simple interpretation. For clear-sky conditions, values of the ultraviolet-red irradiance ratio decrease as solar zenith angle increases (Fig. 1e). For a clear-sky tropical atmosphere, the modeled value of $E_d(0^+, 340)/E_d(0^+, 665)$ changes from 0.48 for the sun at nadir to 0.37 for the sun at a zenith angle of 70° . Consistent changes in this ratio are observed for 8–14 January 1993 (Fig. 1e). This sensitivity to solar zenith angle makes the use of this simple ratio as an objective indicator of cloud color problematic.

The spectral structure of the incident irradiance under a variety of cloud conditions may be better quantified using a spectral cloud index, $\text{cl}(\lambda)$, which is calculated in the same manner as the total cloud index $\overline{\text{CL}}$, or

$$\text{cl}(\lambda) = [E_{\text{CS}}(0^+, \lambda) - E_d(0^+, \lambda)]/E_{\text{CS}}(0^+, \lambda). \quad (2)$$

Values of $\text{cl}(\lambda)$ may be interpreted in the same manner as $\overline{\text{CL}}$, where $\text{cl}(\lambda)$ equals 0 under clear-sky conditions while a $\text{cl}(\lambda)$ of 1 represents a totally obscured sky. A graphical representation of the dependence of the observed spectral cloud index, $\text{cl}(\lambda)$, on wavelength and on the total cloud index $\overline{\text{CL}}$ illustrates the importance of cloud color on visible and near-ultraviolet incident irradiance (Fig. 4). When the total solar flux is reduced by a factor of 2 ($\overline{\text{CL}} = 0.5$), the near-ultraviolet wavebands are reduced by only 35% [$\text{cl}(380) \approx 0.35$] while the red wavebands are reduced by the same amount as the total solar flux [$\text{cl}(685) \approx 0.50$]. Thus, there is an approximate 15% enhancement of incoming radiation in the near-ultraviolet relative to the total flux due to the fact that clouds are more “transparent” to near-ultraviolet radiation than for either red or total solar fluxes. This also indicates that the near-infrared spectrum ($\lambda \geq 700 \text{ nm}$) must be preferentially reduced due to the presence of clouds.

The apparent relationships among the spectral and

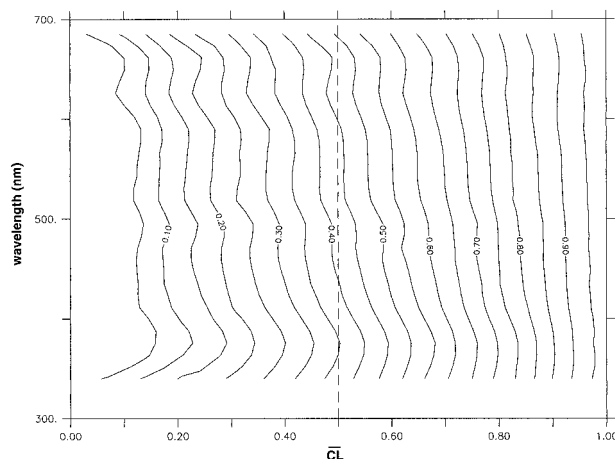


FIG. 4. Contoured distribution of the mean spectral cloud index $\text{cl}(\lambda)$ vs the total cloud index $\overline{\text{CL}}$ and wavelength λ . The dashed vertical line represents a $\overline{\text{CL}}$ of 0.5. All available wavebands (13 bands between 340 and 683 nm) are used to make this contoured data distribution.

total cloud indices, $\text{cl}(\lambda)$ and $\overline{\text{CL}}$, suggest that a simple linear model for $\text{cl}(\lambda)$ with respect to wavelength will explain much of the spectral structure of $\text{cl}(\lambda)$. In Fig. 5, the spectral dependence of $\text{cl}(\lambda)$ is shown for bins of $\overline{\text{CL}}$ values ranging from 0.1 to 0.9 (with bin ranges, $\Delta\overline{\text{CL}}$, equal to 0.01). For $\overline{\text{CL}}$ values greater than ~ 0.3 , the spectral dependence of $\text{cl}(\lambda)$ is very well explained by a simple linear relationship ($r^2 \geq 0.75$). For all of the $\overline{\text{CL}}$ bins, the value of $\text{cl}(\lambda)$ and $\overline{\text{CL}}$ are roughly equal at a wavelength of about 700 nm and estimates of $\text{cl}(\lambda)$ decrease with decreasing λ . For the near-ultraviolet and blue spectral regions, determinations of $\text{cl}(\lambda)$ are lower than $\overline{\text{CL}}$ by as much as 0.2. Values of $\text{cl}(\lambda)$ are not significantly different from $\overline{\text{CL}}$ when the value of $\overline{\text{CL}}$ is negative [for the $\overline{\text{CL}} = -0.01$ bin, the slope of the regression between $\text{cl}(\lambda)$ and λ is not different from zero ($r^2 = 0.00$)]. This suggests that the “color” of the incident irradiance spectrum of a $\overline{\text{CL}} \leq 0$ sky is the same as that of a clear sky.

The observed linear spectral dependence in $\text{cl}(\lambda)$ for constant values of $\overline{\text{CL}}$ indicates that a linear regression model is appropriate for modeling the spectral structure of $\text{cl}(\lambda)$ in terms of the total cloud index $\overline{\text{CL}}$, or

$$\widehat{\text{cl}}(\lambda; \overline{\text{CL}}) = A(\overline{\text{CL}}) \lambda + B(\overline{\text{CL}}), \quad (3)$$

where $A(\overline{\text{CL}})$ and $B(\overline{\text{CL}})$ are constants of the regression model for each $\overline{\text{CL}}$ band ($\Delta\overline{\text{CL}} = 0.01$). The linear model for $\text{cl}(\lambda)$ versus λ is used rather than a quadratic relationship (Nann and Riordan 1991) as it is most consistent with the observations (Fig. 5). Values of the regression constants $A(\overline{\text{CL}})$ and $B(\overline{\text{CL}})$ and squared correlation coefficients for each regression are shown in Fig. 6. Values of $A(\overline{\text{CL}})$ are at their greatest when $\overline{\text{CL}}$ is equal to 0.5 and a linear relationship explains more than 80% of the observed variance when $\overline{\text{CL}}$ is greater than ~ 0.3 . The $\overline{\text{CL}}$ dependence for $A(\overline{\text{CL}})$ and $B(\overline{\text{CL}})$

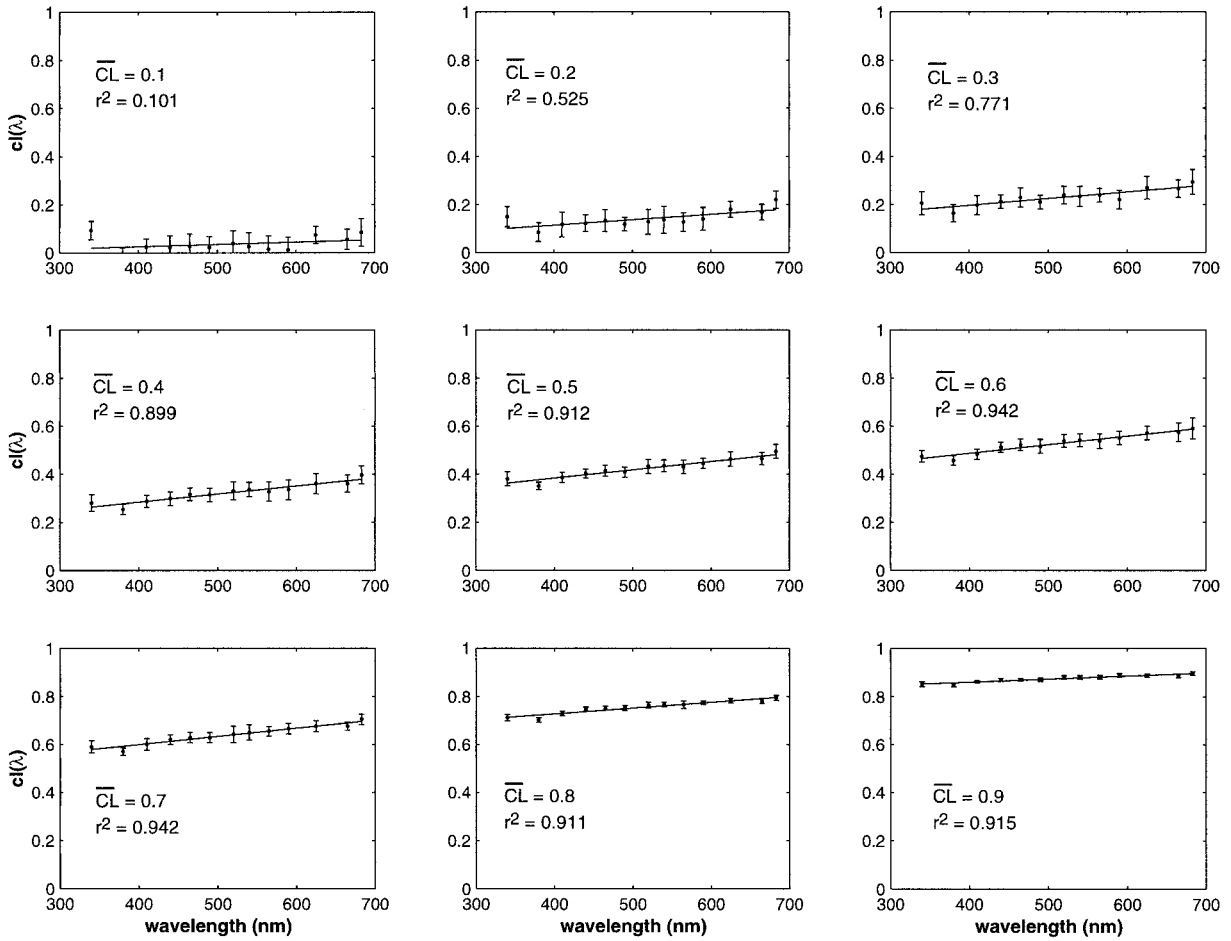


FIG. 5. Examples of the observed spectral dependency of $c_l(\lambda)$ on \overline{CL} . Linear regressions are calculated between $c_l(\lambda)$ and λ for \overline{CL} values ranging from 0.1 to 0.9 for a bin size, $\Delta\overline{CL}$, of 0.01. Also shown is the square correlation coefficient for the $\widehat{c_l}(\lambda; \overline{CL})$ regression model [Eq. (3)]. Error bars for each $c_l(\lambda)$ shown represent standard deviation envelopes for the mean $c_l(\lambda)$ value for each \overline{CL} bin.

can be well explained using a quadratic parameterization, or

$$A(\overline{CL}) = 0.00150\overline{CL}(1 - \overline{CL}) \quad r^2 = 0.959 \quad (4a)$$

$$B(\overline{CL}) = 0.966\overline{CL}^2 + 0.0619\overline{CL} - 0.0389 \quad r^2 = 0.998. \quad (4b)$$

These relationships [Eqs. (2), (3), and (4)] provide a simple empirical parameterization for the incident irradiance spectrum under cloudy conditions, $\hat{E}_d(0^+, \lambda)$, knowing only the total solar flux $\overline{E}_d(0^+)$ and a representative clear-sky spectrum, $E_{CS}(0^+, \lambda)$, or

$$\begin{aligned} \hat{E}_d(0^+, \lambda) &= E_{CS}(0^+, \lambda)[1 - \widehat{c_l}(\lambda; \overline{CL})] \\ &= E_{CS}(0^+, \lambda)[1 - A(\overline{CL})\lambda - B(\overline{CL})]. \end{aligned} \quad (5)$$

Values of $\widehat{c_l}(\lambda; \overline{CL})$ are set to the value of \overline{CL} when $\overline{CL} \leq 0$ as the spectral slope $A(\overline{CL})$ is not statistically different from 0 (at the 95% c.i.) for values of \overline{CL} are less than 0 (not shown).

The modeled irradiance spectra $\hat{E}_d(0^+, \lambda)$ explain more than 92% of the variance in the observed incident

spectra (Table 3). The model explains slightly more of the $E_d(0^+, \lambda)$ variance for the near-ultraviolet and blue spectral regions than for the red, which is probably due to the fact that the cloud color effect is more pronounced at these wavelengths. A comparison between the measured $c_l(\lambda)$ and modeled $\widehat{c_l}(\lambda; \overline{CL})$ values illustrates that more than 82% of the variance in cloud color is explained by our simple empirical model. This indicates that changes in the extraterrestrial flux are not driving the high hindcast predictive skills for $\hat{E}_d(0^+, \lambda)$ observed in Table 3. Further, residuals between the parameterized and observed spectral fluxes show no significant correlation with solar zenith angle, fractional cloud cover, or GMS cloud-top temperature.

5. Radiative transfer modeling of the cloud color phenomenon

In order to evaluate the cloud parameters that are driving the observed changes in cloud color and to assess the global validity of our observation results, we

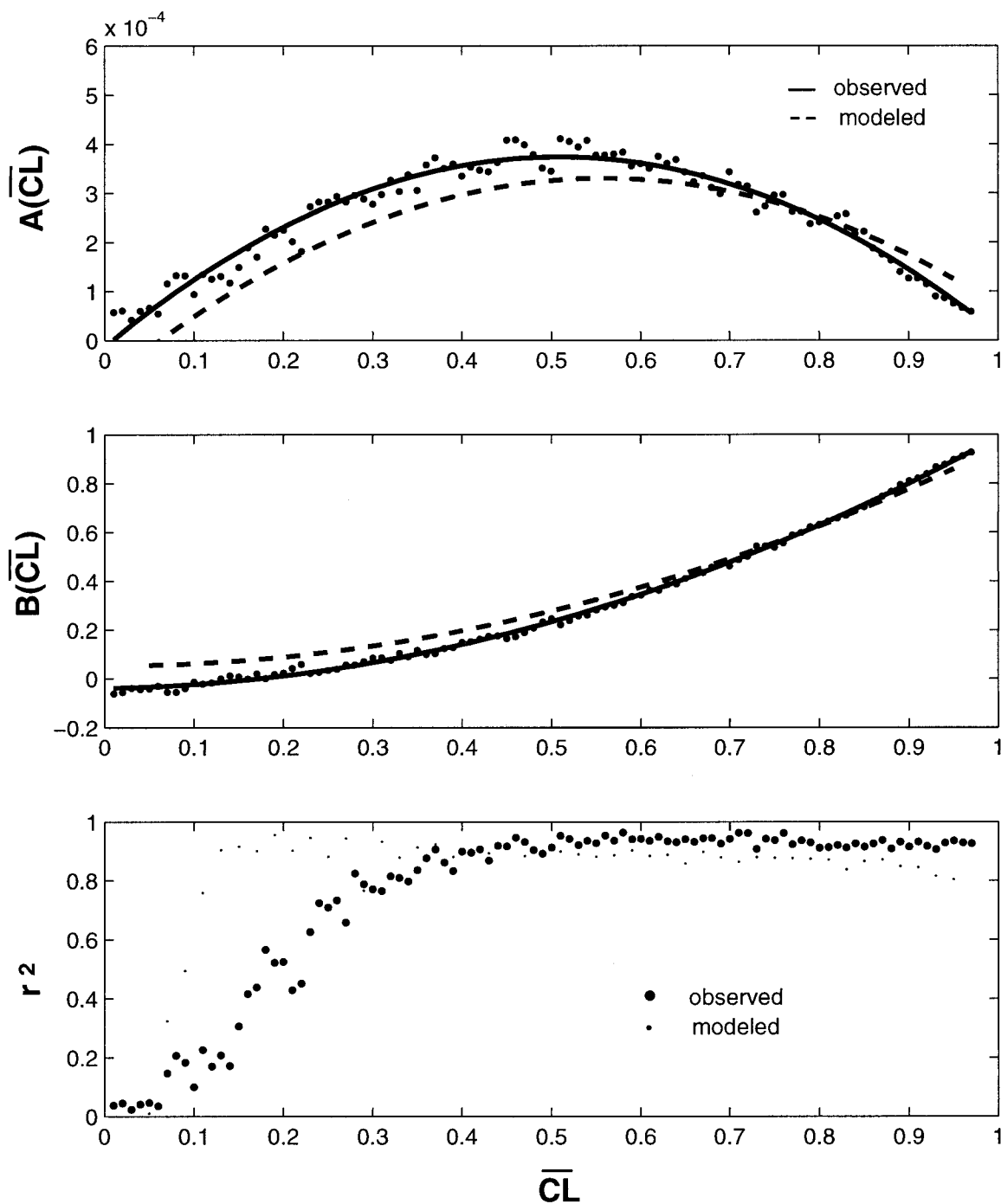


FIG. 6. Regression coefficients for the linear spectral model for $cl(\lambda)$ vs \overline{CL} from Eq. (3). The upper to lower panels show the slope of the linear spectral model, $A(\overline{CL})$, the offset of the linear model, $B(\overline{CL})$, and the squared correlation coefficient for the individual spectral fits. Also shown are the quadratic fits for the observed $A(\overline{CL})$ and $B(\overline{CL})$ (solid line) and the SBDART modeled $A_{mod}(\overline{CL})$ and $B_{mod}(\overline{CL})$ (dashed line) coefficients. The full analytic expressions for $A(\overline{CL})$ and $B(\overline{CL})$ and for $A_{mod}(\overline{CL})$ and $B_{mod}(\overline{CL})$ may be found in Eqs. (4) and (6), respectively.

use the plane-parallel cloud radiative transfer model of Ricchiuzzi et al. (1998; SBDART) to simulate typical cloudy-sky irradiance spectra for the entire solar spectrum. It is not expected that the SBDART modeled ir-

radiance spectra will exactly mimic the at-sea observations. However, the model simulations help in developing a more complete understanding of the cloud color phenomenon and its oceanographic implications.

TABLE 3. Hindcast skills for the modeled cloudy-sky irradiance spectra. The $E_d(0^+, \lambda)$ comparison gives the r^2 values between the measured and modeled $E_d(0^+, \lambda)$ while the $cl(\lambda)$ comparison compares the measured and modeled spectral cloud indices. All of the data are used in these comparisons where the number of data points is equal to 41 900.

Waveband (nm)	$E_d(0^+, \lambda)$ comparison	$cl(\lambda)$ comparison
340	0.947	0.834
380	0.945	0.849
410	0.941	0.853
440	0.939	0.852
465	0.939	0.849
490	0.935	0.846
520	0.933	0.840
540	0.933	0.840
565	0.932	0.834
590	0.932	0.835
625	0.929	0.830
665	0.926	0.826
683	0.924	0.826

An example of SBDART modeled clear- and cloudy-sky irradiance spectra is shown in Fig. 7. These spectra are modeled for a standard tropical clear-sky atmosphere with a solar zenith angle of 40° . For the cloudy-sky spectrum, the cloud optical thickness (at 550 nm) was set to 10, resulting in a \overline{CL} value of 0.49. As expected, the magnitude of the cloudy-sky irradiance is much less than the clear-sky spectrum (Fig. 7a). Determinations of $cl(\lambda)$ show the cloud color effect where values of $cl(\lambda)$ in the visible and ultraviolet regions of the spectrum are significantly less than the mean value of \overline{CL} (Fig. 7b). In addition, values of $cl(\lambda)$ are much larger than \overline{CL} for wavelengths greater than 800 nm and a significant degree of curvature is found for $cl(\lambda)$ within the ultraviolet and visible regions (Fig. 7b; Nann and Riordan 1991). Our empirical $cl(\lambda)$ model [Eqs. (3) and (4)] assumes that $cl(\lambda)$ is a linear function of wavelength over the range of measurements (340–683 nm; Fig. 6). The curvature in the modeled $cl(\lambda)$ spectrum does suggest that applying our simple empirical model out of its wavelength bounds may underestimate the cloud color effect in the ultraviolet, particularly in the UV-B region of the spectrum ($280 < \lambda < 320$ nm).

The power of the radiative transfer model is that it enables us to evaluate the parametric sensitivities of \overline{CL} and $cl(\lambda)$ due to cloud geometric and microphysical parameters as well as solar illumination geometry. After evaluating a large number of simulations ($N > 2000$), we found that, over the visible and ultraviolet spectrum, values of \overline{CL} are strongly dependent upon the cloud optical thickness at 550 nm, τ_{cl} , and to a lesser degree on the solar zenith angle θ . Changes in the plane-parallel cloud configuration (cf. base height, thickness, etc.) or the effective cloud droplet radius had little noticeable effects on estimates of \overline{CL} (results not shown). A graphical representation of the SBDART modeled relationship distribution of \overline{CL} as a function of τ_{cl} and θ is

shown in Fig. 8. This depiction illustrates that \overline{CL} is a strong function of τ_{cl} and a significantly weaker function of θ , especially for larger values of τ_{cl} . For a given value of τ_{cl} , the modeled values of \overline{CL} vary by less than 0.15 when evaluated over the entire range of θ .

The modeled spectral distribution of $cl(\lambda)$ (Fig. 9) shows many of the same features found in the observational dataset (Fig. 4). Values of $cl(\lambda)$ in the ultraviolet and blue visible spectral regions are less than values found in the red by roughly 12% when \overline{CL} equals 0.5. The modeled cloud color differences are slightly less than those observed (Figs. 4 and 9). However, the fact that the same basic distributions are found for both the modeled and the observed datasets is encouraging.

The empirical linear spectral model for $cl(\lambda)$ [Eq. (4)] may also be assessed by evaluating the SBDART results in an identical fashion to the observations. For this calculation, all SBDART simulations are used and linear fits between $cl(\lambda)$ and λ are produced for a given band of \overline{CL} values ($\Delta\overline{CL} = 0.02$). The squared correlation coefficients for the linear fits are greater than 0.8 for \overline{CL} values greater than ~ 0.1 , indicating again that the linear model works well for the range of wavelengths utilized (the small dots in the bottom panel of Fig. 6). The values of the SBDART evaluated regression constants, $A_{mod}(\overline{CL})$ and $B_{mod}(\overline{CL})$, are surprisingly consistent with those determined from the observations (dashed lines in the top two panels of Fig. 6). As before, the greatest change in $cl(\lambda)$ occurs when \overline{CL} is approximately equal to 0.5 and a simple quadratic parameterization can be used to model the dependence of $A_{mod}(\overline{CL})$ and $B_{mod}(\overline{CL})$ on \overline{CL} , or

$$A_{mod}(\overline{CL}) = -0.00130\overline{CL}^2 + 0.0015\overline{CL} - 0.0001$$

$$r^2 = 0.834 \quad (6a)$$

$$B_{mod}(\overline{CL}) = 0.887\overline{CL}^2 + 0.0061\overline{CL} + 0.0562$$

$$r^2 = 0.992. \quad (6b)$$

The \overline{CL} -based parameterization of the radiative transfer model results is consistent with results derived from our observational dataset [Eq. (4) and Fig. 6]. This suggests that the cloud color signal is well modeled using a plane-parallel cloudy-sky radiative transfer model.

We assert that the cloud color signal is, in large part, independent of the 3D micro- and macrophysical characteristics of the overlying clouds and can be accurately modeled using the simpler plane-parallel assumption. The quantitative similarity between the observationally and model-derived $cl(\lambda)$ parameterizations support this assertion. Further, recent radiative transfer calculations through fully 3D clouds show little significant differences between the cloud color signal modeled using the plane parallel and 3D cloud geometry (O'Hirok and Gautier 1998a,b). This indicates that we can use plane-parallel cloudy-sky model results for assessing the oceanic implications of the cloud color phenomenon.

6. Modeling upper-ocean radiant heating rates

The radiant heating of the upper ocean can be determined knowing the divergence of the net irradiance vector within the water column, or

$$\text{RHR}(H) = \frac{\overline{E}_n(0^-) - \overline{E}_n(H)}{\rho c_p H}, \quad (7)$$

where $\text{RHR}(H)$ is the radiant heating rate for a water column of depth H ; $\overline{E}_n(0^-)$ is the net total solar irradiance just beneath the sea surface and $\overline{E}_n(H)$ is that same quantity at a depth, H ; ρ is the in situ seawater density ($\sim 1025 \text{ kg m}^{-3}$); and c_p is the specific heat of seawater ($\sim 4050 \text{ J kg}^{-1} \text{ K}^{-1}$; e.g., Morel and Antoine 1994; Siegel et al. 1995a; Ohlmann et al. 1996; Ohlmann et al. 1998). The net irradiance just beneath the sea surface can be determined knowing the incident irradiance $E_d(0^+, \lambda)$ and sea surface albedo $\alpha(\lambda)$ spectra, or

$$\overline{E}_n(0^-) = \int_{\lambda_{\text{solar}}} (1 - \alpha(\lambda)) E_d(0^+, \lambda) d\lambda, \quad (8a)$$

where the spectral integration is over the entire solar spectrum (250–2500 nm). Similarly, the net irradiance at depth H can be determined knowing the rate at which the in situ downwelling irradiance spectrum diminishes with depth, the diffuse attenuation coefficient spectrum $K_d(z, \lambda)$, or

$$\begin{aligned} \overline{E}_n(H) = & \int_{\lambda_{\text{solar}}} (1 - \alpha(\lambda)) E_d(0^+, \lambda) \\ & \times \exp\left(-\int_{0^+}^H K_d(z', \lambda) dz'\right) d\lambda. \end{aligned} \quad (8b)$$

Thus knowing the vertical profile of the diffuse attenuation coefficient spectrum, the sea surface albedo spectrum, and the incident irradiance spectrum, the net flux of solar radiation at depth [Eq. (8b)] and the radiant heating rate of a layer [Eq. (7)] can be determined.

A convenient way for quantifying the in-water flux of solar radiation independent of the value of the incident flux is to define a depth-dependent transmission function, $\text{Tr}(H)$, that relates the net solar flux at depth, $\overline{E}_n(H)$, to the total downwelling solar flux at the sea surface, $\overline{E}_d(0^+)$ (Siegel et al. 1995a; Ohlmann et al. 1998), or

$$\text{Tr}(H) = \overline{E}_n(H) / \overline{E}_d(0^+), \quad (9a)$$

where the definition of $\text{Tr}(H)$ includes the effects of the sea surface albedo [i.e., $\text{Tr}(0) = 1 - \overline{\alpha}$]. Knowing $\text{Tr}(H)$, the radiant heating rate can be determined as

$$\text{RHR}(H) = \frac{\overline{E}_d(0^+)}{\rho c_p H} [1 - \overline{\alpha} - \text{Tr}(H)], \quad (9b)$$

where the spectrally averaged sea surface albedo $\overline{\alpha}$ is assumed to be equal to 0.06 (e.g., Payne 1972).

In order to calculate values of solar radiation transmission and radiant heating rates, we need to estimate the value of the diffuse attenuation coefficient spectrum $K_d(z, \lambda)$. We model values of $K_d(z, \lambda)$ using the bio-optical algorithm of Morel and Antoine (1994) that parameterizes the depth-independent $K_d(\lambda)$ spectrum as a function of the chlorophyll concentration over a spectral range of 300–2500 nm. This model assumes that the light attenuating properties of the ocean can be explained by a single bio-optical index, the chlorophyll pigment concentration. The Morel and Antoine (1994) bio-optical model was chosen over other models as it resolves the entire solar spectrum. The Morel and Antoine (1994) $K_d(\lambda)$ spectrum is shown in Fig. 7c for chlorophyll concentrations of 0.05, 0.5, and 5 mg m^{-3} and for a solar zenith angle of 40° . A broad minimum in $K_d(\lambda)$ is observed between 350 and 500 nm associated with the most penetrating wavelengths. It is in this penetrating waveband where chlorophyll concentrations have their greatest influence on solar radiation attenuation. Outside of the spectral range where significant penetration occurs, values of $K_d(\lambda)$ are much larger and no significant effects of chlorophyll are found. Superimposed in Fig. 7c is the cruise mean $K_d(\lambda)$ spectrum averaged over the upper 40 m from our TOGA COARE in-water observations (Ohlmann et al. 1998). The TOGA COARE $K_d(\lambda)$ observations are most similar to the low chlorophyll (0.05 mg m^{-3}) $K_d(\lambda)$ estimates. For the calculations that follow, the incident irradiance spectrum is taken from the cloudy-sky model results of the previous section (Fig. 7).

For a given value of $\overline{\text{CL}}$, the net flux appears to decrease with depth in an exponential-like fashion and this rate is faster when the chlorophyll concentration is higher (Fig. 10a). It is difficult to separate the effects of changes in the value of the incident flux from changes due to cloud color alone (see the dashed line in Fig. 10a). Values of $\text{Tr}(H)$ show a significant increase with increasing value of the total cloud index, illustrating the importance of cloud color (Fig. 10b). Simply, more of the incident solar spectrum is found within the penetrating spectral region for seawater (Fig. 7). At a depth of 10 m and a chlorophyll concentration of 0.05 mg m^{-3} , the value of $\text{Tr}(10 \text{ m})$ increases from $\sim 21\%$ to roughly 30% across the full range of $\overline{\text{CL}}$ values (Fig. 10b). The range of estimates for the net radiant flux at 10 m simply due to the cloud color changes in the specification of $\text{Tr}(H)$ is 20 W m^{-2} (assuming a climatological value of incident irradiance of 220 W m^{-2} ; Ohlmann et al. 1996). For higher chlorophyll concentrations, these cloud color-induced changes in $\text{Tr}(10 \text{ m})$ will be considerably smaller. For shallow depths ($H = 0.1 \text{ m}$), these effects will be quite large and roughly independent of the chlorophyll concentration [i.e., $\text{Tr}(0.1 \text{ m})$ changes by more than 15% over the full range of $\overline{\text{CL}}$; Fig. 10b].

Changes of the sea surface temperature (SST) are regulated to a large degree by the absorption of radiant energy in the upper few meters of the water column

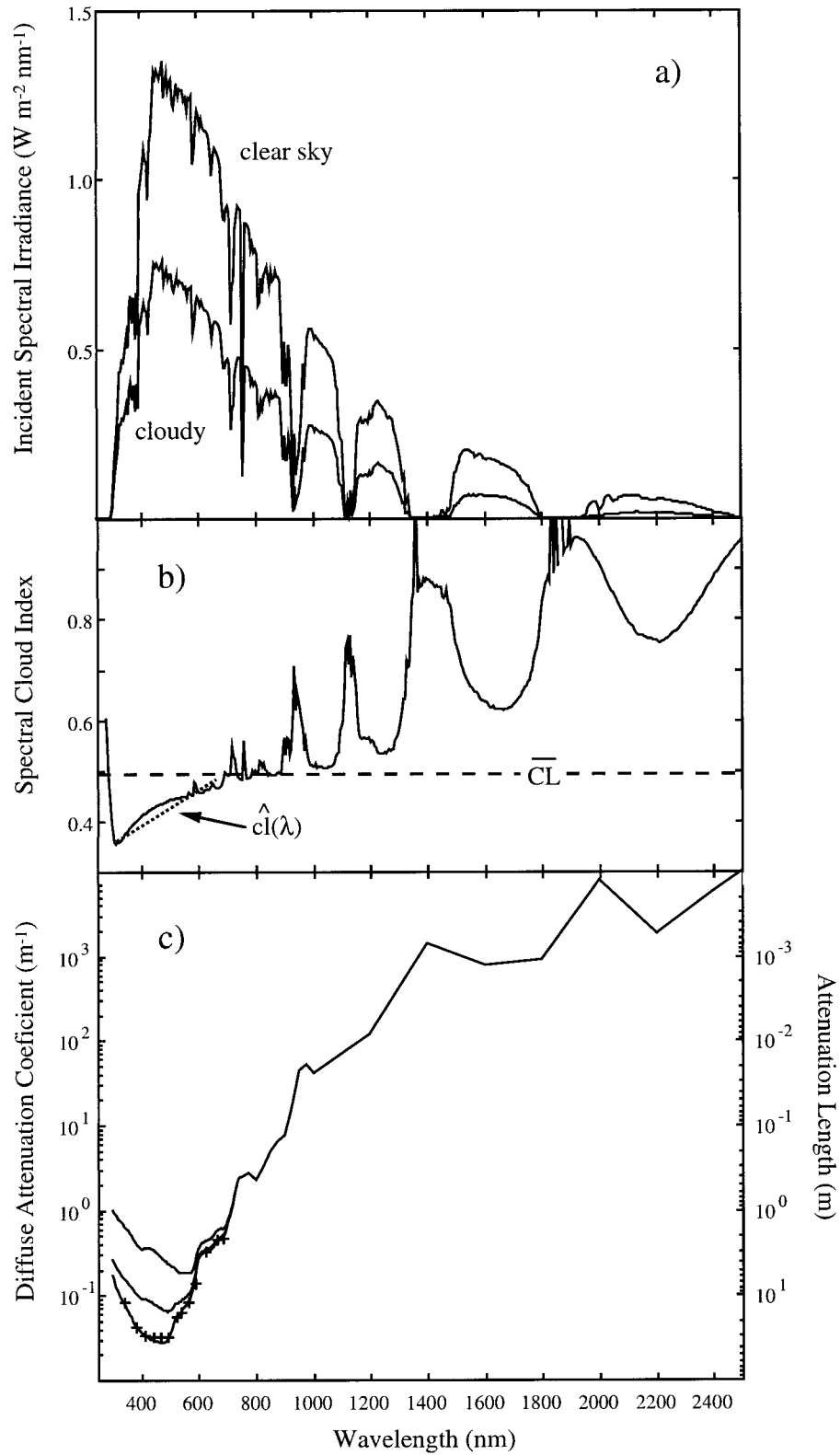


FIG. 7. An example of full-spectral (250–2500 nm) distributions for (a) downwelling irradiance spectra for clear-sky and cloudy conditions, (b) spectral cloud index $\text{cl}(\lambda)$, and (c) estimates of the diffuse attenuation coefficient spectrum ($K_d(\lambda)$) for chlorophyll concentrations of 0.05, 0.5, and 5 mg m^{-3} . A standard tropical clear-sky atmosphere is assumed along with a solar zenith angle of 40° for both spectra. A single

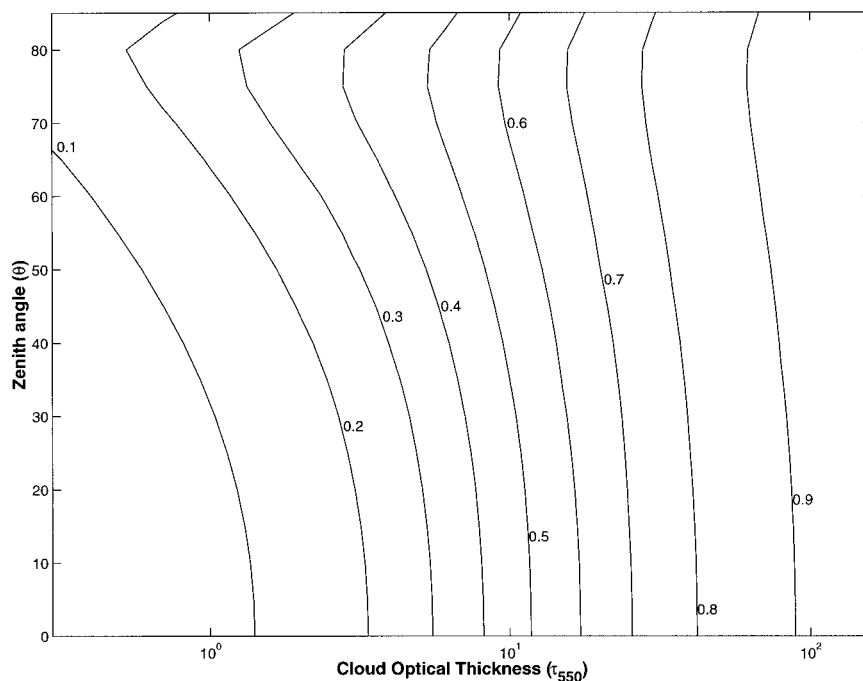


FIG. 8. Contoured distribution of the SBDART modeled \overline{CL} values as a function of the cloud optical thickness (at 550 nm) and the solar zenith angle. A single 2-km-thick cloud layer with a base height of 1 km, an effective cloud droplet radius of 25 μm , and a standard tropical clear-sky atmosphere are assumed. Changes in cloud geometric factors, effective cloud droplet radius, or clear-sky characteristics had little effect upon the resulting determinations of \overline{CL} .

(e.g., Denman 1973). In order to best evaluate the importance of clouds on the modeling of near-surface radiant heating rates, we scale each $RHR(H)$ estimate to the climatological value for incident solar flux (220 W m^{-2}). In this way, we assess the importance of cloud color on the specification of radiant heating rates independent of changes in the incident flux. Modeled values of $RHR_{\text{scale}}(0.1 \text{ m})$ decrease with increasing cloud index from $\sim 14 \text{ K day}^{-1}$ for a clear-sky to 7 K day^{-1} when \overline{CL} is equal to 0.9 (Fig. 10c). As H increases, the effects of \overline{CL} on $RHR_{\text{scale}}(H)$ are damped significantly. Differences in the chlorophyll pigment concentration have little role in determining the value of $RHR_{\text{scale}}(H)$. These changes are large and will be important for the proper specification of the near-surface warm layer in SST calculations (e.g., Fairall et al. 1996; Ohlmann 1997).

The model results demonstrate that clouds affect the transmission of solar radiation to depth as well as the rate of radiant heating of the near-surface ocean. The observed role of clouds is beyond the simple altering of the total incident solar flux. The proper specification

of the cloud color effect will be important for estimating the time rate of change of mixed layer heat content (e.g., Ohlmann et al. 1996; Anderson et al. 1996) as well as for understanding the processes that regulate the formation of the near-surface diurnal warm layer (e.g., Webster et al. 1996; Fairall et al. 1996). Thus, the proper specification of in-water radiation properties with respect to cloud color is an important, yet still unaccounted for, factor in air-sea interaction calculations.

7. Observations of cloud color regulation of solar radiation penetration

One of the primary objectives of this contribution is to evaluate the effects of cloud color on ocean radiant heating. Unfortunately, it is extremely difficult to make accurate irradiance measurements of the entire solar spectrum (250–2500 nm) within the upper few meters of the ocean from a standard research vessel. The TOGA COARE in-water optics observations concentrated on the determination of the net solar flux exiting the near-surface mixed layer (Siegel et al. 1995a; Ohlmann et

←

2-km-thick cloud layer (1-km base height) with a cloud optical thickness of 10 (at 550 nm) and effective cloud droplet radius of 25 μm is used to drive the cloudy-sky radiative transfer model. The total cloud index \overline{CL} for this example is 0.49. (b) The dotted line represents the empirical $\widehat{CL}(\lambda; \overline{CL})$ regression model [Eq. (3)]. (c) The Morel and Antoine (1994) full spectral $K_d(\lambda)$ parameterization is used and the “+” symbols show cruise mean $K_d(\lambda)$ observations for the upper 40 m of the TOGA COARE dataset (Ohlmann et al. 1998).

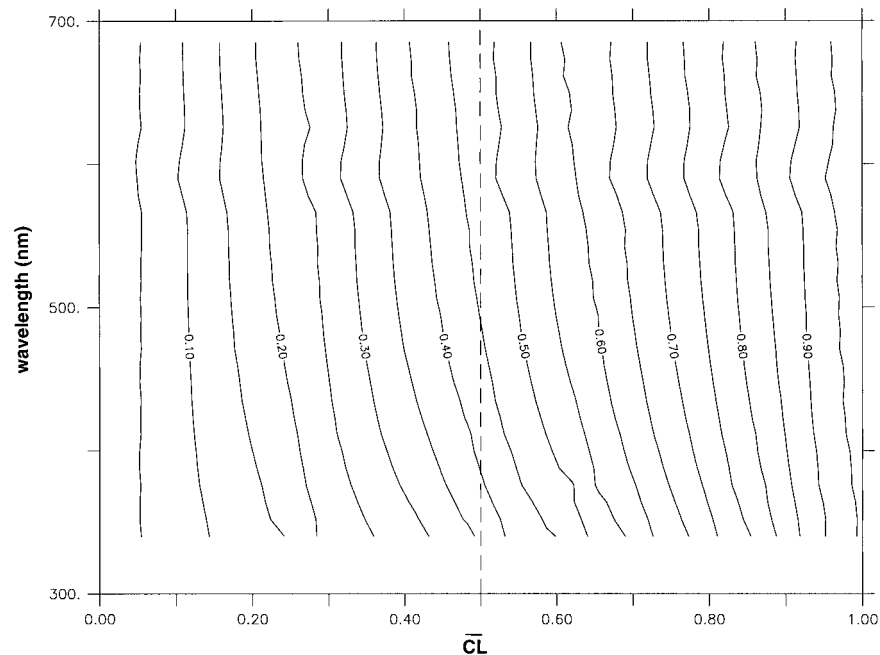


FIG. 9. Spectral distribution of the SBDART modeled $cl(\lambda)$ estimates as a function of \overline{CL} . All solar zenith angles (0° – 85° in 5° increments) and cloud optical thickness cases simulated are used to make this determination.

al. 1998). These spectral measurements span the expected solar spectrum at depths greater than 10 m (350–700 nm) and hence are not appropriate for evaluating near-surface ($H < 10$ m) radiant heating rates. However, they can be used to quantify the role of clouds on the transmission of the in-water flux of solar radiation, $Tr(H)$. In an earlier contribution (Siegel et al. 1995a), we demonstrated that values of $Tr(H)$ decrease in a near-exponential fashion with depth (for $H \geq 10$ m) and that the rate of decrease was strongly dependent upon the upper-ocean chlorophyll concentration. However, there remained a great deal of unexplained variability in the cruise mean estimates of $Tr(z)$ (Siegel et al. 1995a; Ohlmann et al. 1998).

In order to assess the role of clouds on solar radiation penetration, we partition the TOGA COARE time series into periods of high and low chlorophyll concentrations to account for changes in $Tr(H)$ due to chlorophyll concentration changes (see Fig. 4 in Siegel et al. 1995a). This allows the effects of clouds on $Tr(H)$ to be evaluated nearly independently of chlorophyll. The mean value of the chlorophyll a concentrations averaged over the upper 40 m is $0.090 (\pm 0.015 \text{ std dev}) \text{ mg m}^{-3}$ for low chlorophyll conditions and $0.217 (\pm 0.034 \text{ std dev}) \text{ mg m}^{-3}$ for high chlorophyll periods.

Mean vertical profiles of $Tr(H)$ for high cloud ($\overline{CL} > 0.7$) and low cloud ($\overline{CL} < 0.3$) indices for both high (solid) and low (dashed) chlorophyll conditions are shown in Fig. 11. The mean $Tr(H)$ profiles for the high \overline{CL} cases are significantly larger (i.e., they lie to the right of the clear-sky cases in Fig. 11), indicating that

a greater portion of the incident solar flux propagates to depth under cloudy-sky conditions. At 10 m, the difference due to clouds alone is 4% for both chlorophyll cases, while at depth, the cloud-induced differences disappear. Assuming a climatological estimate for $\overline{E}_d(0^+)$, these data show that the daily mean net solar flux at 10 m will increase by $\sim 9 \text{ W m}^{-2}$ simply due to whether cloud color is included in the specification of $Tr(H)$.

The dependence of $Tr(H)$ on depth, clouds, and chlorophyll can be conceptualized using the data presented in Fig. 11. For example, at 10 m, differences among the four mean $Tr(10 \text{ m})$ determinations are due to \overline{CL} , whereas at a depth of 30 m, the value of $Tr(30 \text{ m})$ is primarily controlled by chlorophyll. Uncertainties of this magnitude for solar radiation penetration must be resolved if we are to successfully close air–sea heat budgets for the western tropical Pacific Ocean (e.g., Godfrey and Lindstrom 1989).

8. Summary and conclusions

We have demonstrated the existence of the cloud color phenomenon using both field observations and atmospheric radiative transfer model simulations and have assessed its implications for ocean radiant heating. Specifically, we show that the flux of near-ultraviolet through green solar radiation is significantly enhanced relative to the total incident flux under a cloudy sky. An empirical parameterization of the spectral cloud indices in terms of the total cloud index is developed and verified using results from a plane-parallel cloudy-sky

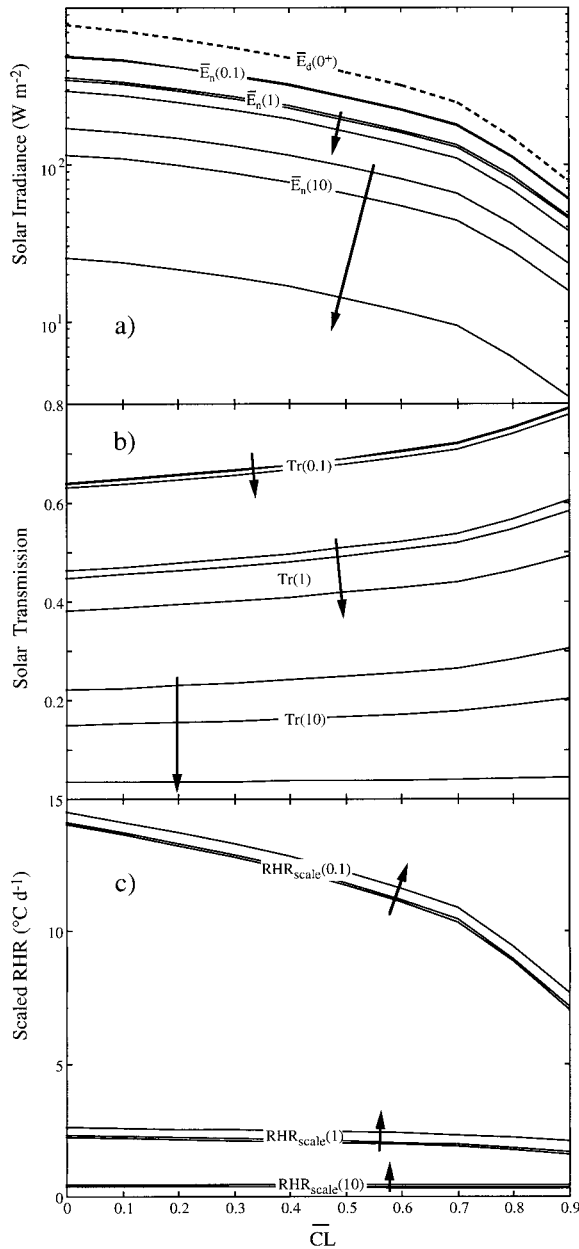


FIG. 10. Modeled estimates of (a) incident and in-water solar fluxes ($W m^{-2}$), (b) transmission function [$Tr(z)$], and (c) the upper-layer radiant heating rate ($K day^{-1}$) scaled to a climatological mean incident flux ($220 W m^{-2}$) for depths of 0.1, 1, and 10 m and chlorophyll concentrations of 0.05, 0.5, and $5 mg m^{-3}$. (a) Incident solar flux $\bar{E}_d(0^+)$ is shown as the dashed line. The arrows indicate the direction of increasing chlorophyll concentration for each set of depths.

atmospheric radiative transfer model. We show that the radiant heating rate of the upper 10 cm of ocean (normalized to the climatological incident solar flux) is reduced by a factor of 2 due to the presence of clouds and that the transmission of solar radiation within the water column significantly increases due to the presence of clouds, particularly in the upper 20 m.

The present results strongly indicate that the cloud

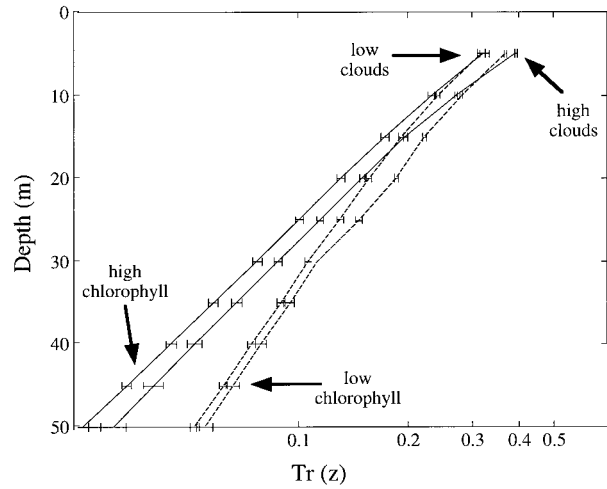


FIG. 11. Mean vertical profiles of $Tr(z)$ under high (solid) and low (dashed) chlorophyll concentration conditions for high ($\overline{CL} \geq 0.7$) and low cloud ($\overline{CL} < 0.3$). The high \overline{CL} cases lie to the right of the low ones for each pair of chlorophyll concentration. Mean values of chlorophyll *a* concentration in the upper 40 m of the water column are equal to $0.090 (\pm 0.016 \text{ std dev}) mg m^{-3}$ for low chlorophyll conditions and $0.217 (\pm 0.034 \text{ std dev}) mg m^{-3}$ for high chlorophyll periods. At least 116 (19) individual profiles compose the high chlorophyll mean estimates for clear (cloudy) \overline{CL} conditions. For the low chlorophyll case, 229 (69) profiles are used for clear-sky (cloudy sky) \overline{CL} conditions. The error bars represent 95% confidence intervals for the individual mean estimates.

color phenomenon must be included in the modeling of ocean radiant heating rates. This factor has yet to be included in any formulation of ocean radiant heating. For example, most oceanic applications model the net flux at depth $\bar{E}_n(H)$ as the sum of several to many independent spectral bands, or

$$\bar{E}_n(H) = (1 - \bar{\alpha})\bar{E}_d(0^+) \sum_{j=1}^{N_\lambda} A_j \exp(-K_j H), \quad (10)$$

where $\bar{\alpha}$ is the spectral mean sea surface albedo, N_λ is the number of distinct spectral bands used to model the solar flux, A_j is the fraction of the total incident irradiance found in each spectral band, and K_j is the vertical attenuation coefficient for each waveband. Variations of the K_j parameter are well understood and modeled either using the observed chlorophyll concentration (e.g., Smith and Baker 1978; Morel and Antoine 1994; Ohlmann et al. 1996) or by applying the subjective ‘‘Jerlov-type’’ index of water clarity (e.g., Jerlov 1976; Paulson and Simpson 1977; Woods et al. 1984). However, the quantity A_j is always assumed to be a constant. The present results indicate that the A_j parameter should vary with cloud conditions. More research is clearly needed to develop an all-weather parameterization for solar radiation penetration and radiant heating for use in air-sea interaction analyses and models.

The present results provide an interesting conceptualization of the role of clouds in determining ocean heating rates. To zeroth order, clouds regulate the amount of solar radiation reaching the sea surface. This gov-

erning of the total solar flux is, of course, the major factor controlling the input of heat into the sea. However, once solar radiation enters the sea, the specification of the net radiative flux within the water column and its vertical divergence is also dependent upon clouds. We can compartmentalize the role of solar radiation in thermal climate into two distinct processes: the absorption of solar energy near the sea surface, which is associated with changes in SST; and the penetration of solar radiation to depth, which influences the heat content of the mixed layer. The presence or absence of clouds governs which of the two "roles" is active. In broad terms, clear skies will affect SST more, while cloudy skies will increase the relative amount of solar radiation that penetrates to depth. The convolution of the incident solar spectrum with the vertical light attenuation spectrum with the water column regulates this process. The present study indicates that the cloud color phenomenon must be included in the modeling of ocean radiant heating and the transmission of solar radiation within the water column.

Acknowledgments. The authors would like to thank Catherine Gautier, Bill O'Hirok, Paul Ricchiazzi, and Libe Washburn for many discussions and much assistance throughout the course of this work. Shuyi Chen (UW) provided GMS cloud-top temperature data for the location of the R/V *John Vickers*. Detailed comments from the supervising editor (J. A. Coakley Jr.) and the anonymous reviewers greatly improved the manuscript. We gratefully acknowledge support from the National Science Foundation (OCE-91-10556 and OCE-95-25856) and NASA (NAGW-3145).

REFERENCES

- Anderson, S., R. A. Weller, and R. Lukas, 1996: Surface buoyancy forcing and the mixed layer of the western Pacific warm pool: Observations and 1D model results. *J. Climate*, **9**, 3056–3085.
- Byrne, R. N., R. C. K. Somerville, and B. Subasilar, 1996: Broken-cloud enhancement of solar radiation absorption. *J. Atmos. Sci.*, **53**, 878–886.
- Chen, S. S., R. A. Houze Jr., B. E. Mapes, S. R. Brodzik, and S. E. Yuter 1995: TOGA COARE satellite data summaries available on the World Wide Web. *Bull. Amer. Meteor. Soc.*, **76**, 329–333.
- Davis, R. E., 1977: Techniques for statistical analysis and prediction of geophysical fluid systems. *Geophys. Astrophys. Fluid Dyn.*, **8**, 245–277.
- Denman, K. L., 1973: A time-dependent model of the upper ocean. *J. Phys. Oceanogr.*, **3**, 173–184.
- Fairall, C. W., E. F. Bradley, J. S. Godfrey, G. A. Wick, J. B. Edson, and G. S. Young, 1996: Cool-skin and warm-layer effects on sea surface temperature. *J. Geophys. Res.*, **101**, 1295–1308.
- Gautier, C., and R. Frouin, 1992: Net surface solar irradiance variability in the central equatorial Pacific during 1982–1985. *J. Climate*, **5**, 30–55.
- Godfrey, J. S., and E. J. Lindstrom, 1989: The heat budget of the equatorial western Pacific surface mixed layer. *J. Geophys. Res.*, **94**, 8007–8017.
- Jerlov, N. G., 1976: *Marine Optics*. Elsevier, 229 pp.
- Katsaros, K. B., L. A. McMurdie, R. J. Lind, and J. E. DeVault, 1985: Albedo of a water surface: Spectral variation, effects of atmospheric transmittance, sun angle, and wind speed. *J. Geophys. Res.*, **90**, 7313–7321.
- Liou, K.-N., 1980: *An Introduction to Atmospheric Radiation*. Academic Press, 392 pp.
- McClatchey, R. A., R. W. Fenn, J. E. A. Selby, F. E. Volz, and J. S. Garing, 1972: Optical properties of the atmosphere (3d ed.). Air Force Cambridge Research Laboratories Rep. AFCRL-72-0497, 108 pp.
- Middleton, W. E. K., 1954: The color of the overcast sky. *J. Opt. Soc. Amer.*, **44**, 793–798.
- Morel, A., and D. Antoine, 1994: Heating rate within the upper ocean in relation to its bio-optical state. *J. Phys. Oceanogr.*, **24**, 1652–1665.
- Nann, S., and C. Riordan, 1991: Solar spectral irradiance under clear and cloudy skies: Measurements and a semiempirical model. *J. Appl. Meteor.*, **30**, 447–462.
- O'Hirok, W., and C. Gautier, 1998a: A three-dimensional radiative transfer model to investigate the solar radiation within a cloudy atmosphere. Part I: Spatial effects. *J. Atmos. Sci.*, **55**, 2162–2179.
- , and —, 1998b: A three-dimensional radiative transfer model to investigate the solar radiation within a cloudy atmosphere. Part II: Spectral effects. *J. Atmos. Sci.*, **55**, 3065–3076.
- Ohlmann, J. C., 1997: Ocean radiant heating. Ph.D. dissertation, University of California, Santa Barbara, 131 pp.
- , D. A. Siegel, and C. Gautier, 1996: Ocean mixed layer radiant heating and solar penetration: A global analysis. *J. Climate*, **9**, 2265–2280.
- , —, and L. Washburn, 1998: Radiant heating of the western equatorial Pacific during TOGA-COARE. *J. Geophys. Res.*, **103**, 5379–5395.
- Paulson, C. A., and J. J. Simpson, 1977: Irradiance measurements in the upper ocean. *J. Phys. Oceanogr.*, **7**, 953–956.
- Payne, R. E., 1972: Albedo of the sea surface. *J. Atmos. Sci.*, **29**, 959–970.
- Ricchiazzi, P. J., S. Yang, and C. Gautier, 1998: SBDART: A research and teaching software tool for plane-parallel radiative transfer in the earth's atmosphere. *Bull. Amer. Meteor. Soc.*, **79**, 2101–2114.
- Siegel, D. A., and T. D. Dickey, 1987: On the parameterization of irradiance for open ocean photoprocesses. *J. Geophys. Res.*, **92**, 14 648–14 662.
- , J. C. Ohlmann, L. Washburn, R. R. Bidigare, C. Nasse, E. Fields, and Y. Zhou, 1995a: Solar radiation, phytoplankton pigments and the radiant heating of the equatorial Pacific warm pool. *J. Geophys. Res.*, **100**, 4885–4891.
- , D. Konnoff, M. C. O'Brien, J. C. Sorensen, and E. Fields, 1995b: BBOP sampling and data processing protocols. Rep. 19, 77 pp. [Available from U.S. Joint Global Ocean Flux Study Planning and Coordination Office, Woods Hole Oceanographic Institution, Woods Hole, MA 02543.]
- Smith, R. C., and K. S. Baker, 1978: Optical classification of natural waters. *Limnol. Oceanogr.*, **23**, 260–267.
- Webster, P. J., and R. Lukas, 1992: TOGA COARE: The Coupled Ocean–Atmosphere Response Experiment. *Bull. Amer. Meteor. Soc.*, **73**, 1377–1416.
- , C. A. Clayson, and J. A. Curry, 1996: Clouds, radiation, and the diurnal cycle of sea surface temperature in the tropical western Pacific. *J. Climate*, **9**, 1712–1730.
- Woods, J. D., W. Barkmann, and A. Horch, 1984: Solar heating of the oceans: Diurnal, seasonal, and meridional variation. *Quart. J. Roy. Meteor. Soc.*, **110**, 633–656.